



Localized boiling-induced spatters in the high-power laser welding of stainless steel: three-dimensional visualization and physical understanding

Tongtong Liu¹ · Renzhi Hu¹ · Xin Chen¹ · Shuili Gong² · Shengyong Pang¹

Received: 3 June 2018 / Accepted: 19 August 2018 / Published online: 31 August 2018
© Springer-Verlag GmbH Germany, part of Springer Nature 2018

Abstract

Serious spatter defects occur with the intensive interaction between a high-power density laser beam ($> 10^7$ W/cm²) and the material used in high-power (HP) laser welding. In this study, we developed a three-dimensional comprehensive model to physically simulate the keyhole and weld pool dynamics in HP laser welding. Our recent proposed adaptive mesh-refinement method was adopted to solve the model. An interesting phenomenon was directly observed: the intense localized boiling on the mesoscale keyhole wall induced many small spatters (LBiS), sized hundreds of microns, during 10 kW HP laser welding of 304 stainless steel. Experimental studies of parameters were also conducted to validate the model and characterize the spatter behaviors outside the keyhole wall during welding. The theoretical predictions of LBiS behaviors agreed well with the experimental observations. Moreover, the flying directions of LBiS generally approached vertical and were relatively insensitive to welding speed, even when the speed was increased to a very high value of 15 m/min. This finding shows that LBiS are very different from the commonly observed spatter defects produced by the intense friction effect of a vapor plume toward the keyhole, and this finding demonstrates the variety of the spatters. Furthermore, an energy conservation theory was proposed to characterize LBiS, and a novel dimensionless spatter number was formulated to calculate their formation threshold. The spatter number relates to the Reynold and Weber numbers of the molten flow of the weld pool and shows the relative importance of an inertia flow driven by the recoil pressure and the resistance from viscous dissipation, surface tension and gravity. The spatter number was less than 1 when LBiS was formed. The proposed theory was validated against the numerical predictions, and good agreements were obtained.

1 Introduction

Owing to the rapid development of fiber laser science and technology, high-power (HP) fiber lasers have been attracting more industrial attention, since they can be used to join thick or even heavy thick plates with highly efficient one-pass welding. However, welding metals with HP laser are usually prone to the occurrence of spatter defects, even for materials of excellent weldability such as stainless steel [1,

2]. An understanding of the formation mechanisms of spatters is of significance for optimizing the HP laser-welding process of thick plates.

Over the past decades, experimental and theoretical studies were carried out to understand the spatter defects in HP laser welding. Park and Rhee [3] analyzed the relationship between the plasma, the spatter and the bead shape, and discussed the mechanism of spatter formation using online laser-welding monitoring systems. Recently, with the rapid development of HP laser-welding technology, the spatter behaviors have been paid much more attention. Most researchers explained that the high-speed vapor plume was dragging the metal liquid to form spatters. Volpp et al. [4] proposed an analytical model to simulate the keyhole wall movement and found micro-spattering can be formed considering drag forces. Weberpal et al. [5] observed the spray angle of spatters from the keyhole opening using high-speed imaging and proposed that the spatters were mainly induced by the intense friction effects of the vigorous vapor plume

✉ Shengyong Pang
spang@hust.edu.cn

¹ State Key Laboratory of Materials Processing and Die and Mould Technology, Huazhong University of Science and Technology (HUST), Wuhan 430074, People's Republic of China

² Science and Technology on Power Beam Processes Laboratory, AVIC Manufacturing Technology Institute, Beijing, People's Republic of China

evaporated from the front keyhole wall toward the rear keyhole wall. Using advanced micro-focus X-ray imaging, Kawahito et al. [6] proposed that the spatters were caused by the strong shear effect of high-speed vapor plume ejection from the keyhole. Wu et al. [7] also argued that spatters were caused by the low surface tension of molten metal around the keyhole and the strong acceleration of molten metal driven by evaporation and vapor plume shear stress. However, they mainly discussed the formation mechanism of the relatively large-sized spatters based on the simulations with 0.2 mm uniform cells. The dynamic behaviors and mechanisms of the small-size spatters (0.2 mm or smaller) remain unclear due to the resolution limitation of the current simulation method. Very recently, Kaplan et al. [8, 9] determined that there were many types of spattering through experimental observations. They pointed out that the recoil pressure might play an important role in the formation of the spatters. Semak and Matsunawa et al. [10, 11] reported that the enhanced vaporization-induced recoil pressure could induce the ejection of the melt from the interaction zone to form the spatter. Using a sandwich imaging method, Zhang et al. [12] found that the recoil momentum associated with the energized vapor plume jet acting on the keyhole wall might result in the formation of high-speed micro-spatter. The aforementioned investigations deal with various types of spatter and possible formation mechanisms in HP laser welding. However, to our knowledge, the detailed physics that produce spatter in HP laser welding have not been revealed directly and quantitatively. Therefore, the criteria for spatter formation in HP laser welding are still lacking.

In this paper, we systematically investigated the spatter formation process in HP laser welding by a combination of experiments and numerical simulation. A three-dimensional comprehensive model was developed to simulate the

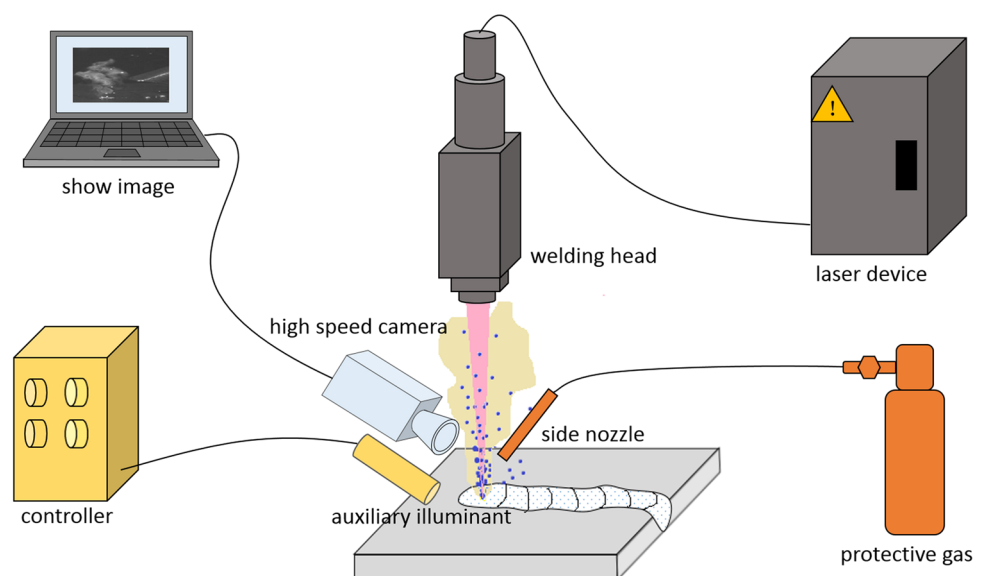
keyhole and weld-pool dynamics in HP laser welding. The octree-based adaptive mesh refinement method was adopted to solve the model. The intense localized boiling of the mesoscale keyhole wall-induced spatters (LBiS) under the circumstance of neglecting the effect of vapor friction was directly and efficiently captured. An energy conservation theory was further proposed to characterize the hundreds of microns size range LBiS and a novel dimensionless spatter number to judge LBiS formation. The spatter number relates to the Reynold and Weber numbers of the molten flow of the weld pool and shows the relative importance of the inertia flow driven by recoil pressure and the resistance from viscous dissipation, surface tension and gravity. This study can help improve understanding of the complicated formation of spatter in HP laser welding.

2 Materials and methods

2.1 Experiments

To observe the behaviors of the spatter flashing out of the keyhole, the bead-on-plate (BOP) welding experiments of the present study were performed. The schematic of the experimental setup is shown in Fig. 1. In the experiments, a high-power fiber laser (IPG YLS-10k, 1080 nm wavelength) was used for welding. The specimens were made of ANSI 304 stainless steel, with a size of 200 mm × 100 mm × 15 mm in the longitudinal, cross section, and penetration directions, respectively. To develop a better understanding of the general spatter behaviors in HP laser welding, we set a wide welding speed range, which was varied from 1 to 15 m/min. The laser power and laser spot focus diameters were fixed as 10 kW and 0.6 mm, respectively. The

Fig. 1 Schematic of the HP laser welding experimental setup



experimental parameters are shown in Table 1. Before welding, the metal sample was rinsed with acetone to remove oxide film and grease. In welding, a high-speed CCD video system (phantom V-Series 611 high-speed camera) was used to observe the spatters' flashing processes. The argon gas was used as a shielding gas to protect the weld, and the gas flow rate was 20 L/min. After welding, the specimens were cut, ground, polished, etched (Kroll reagent: 3–9 mL HCL + 1–3 mL HNO₃, time 6–10 s), and observed with an optical microscope.

2.2 Numerical simulation

In order to understand the spatter's formation mechanisms and the weld pool dynamics in HP laser welding, we numerically simulated the welding process directly, based on our previously developed 3D laser welding model [13, 14]. Considering the facts that there are many different types

of spatters during the laser welding process with different formation mechanisms [8] and a common mechanism of vapor friction inducing spatters has been well studied [4, 5], exploring the other possible mechanisms is needed. For the HP laser welding process, one of the most obvious feature is that the evaporation is quite intense and the resulting recoil pressure drives strong fluid flow. Surface tension may not limit the strongly surface fluid flow. Then, spatter will be formed. Therefore, to understand the possible spatter's formation process quantitatively, an HP laser welding model was developed by invoking the recently improved recoil pressure formula and neglecting the vapor friction effect in the present work. In addition, because the pressure of protective gas on the spatter is very small, its effect is also neglected. Figure 2 represents the studied process.

For the theoretical model, the heat transfer and fluid flow behavior of the molten metal, assumed to be an incompressible fluid, are described as follows [13, 14]:

$$\nabla \cdot \vec{U} = 0, \tag{1}$$

$$\rho \left(\frac{\partial \vec{U}}{\partial t} + (\vec{U} \cdot \nabla) \vec{U} \right) = \nabla \cdot (\mu \nabla \vec{U}) - \nabla p - \frac{\mu}{K} \vec{U} - \frac{C\rho}{\sqrt{K}} |\vec{U}| \vec{U} - \rho \vec{g} \beta (T - T_{ref}), \tag{2}$$

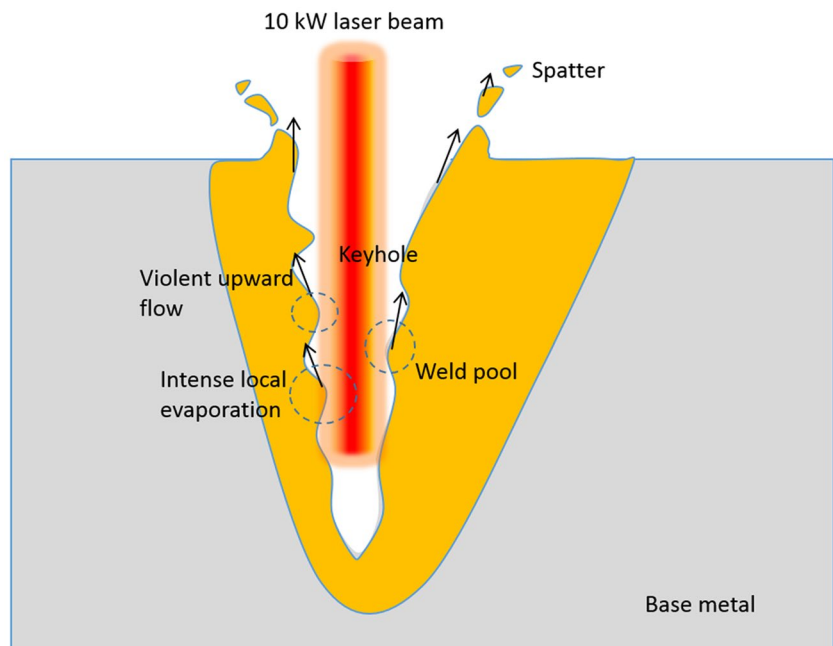
$$\rho C_p \left(\frac{\partial T}{\partial t} + (\vec{U} \cdot \nabla) T \right) = \nabla \cdot (k \nabla T) + Q, \tag{3}$$

where \vec{U} , ρ , p , μ , \vec{g} , T , T_{ref} , β , C_p , and k , respectively, represent the three-dimensional velocity vector, density, pressure,

Table 1 Process parameters used in the experiments

Process number	Laser spot focus diameter (mm)	Laser power (kW)	Welding speed (m/min)
1	0.6	10	1
2	0.6	10	3
3	0.6	10	5
4	0.6	10	7
5	0.6	10	9
6	0.6	10	12
7	0.6	10	15

Fig. 2 Schematic diagram of spatter formation process studied



viscosity, gravity vector, weld pool temperature, reference temperature, coefficient of thermal expansion, heat capacity, and thermal conductivity. Q is the body heat source from laser beam irradiation. C is the inertia parameter associated with the liquid fraction [15]. K is the Carman–Kozeny coefficient of the mixture model [15, 16], which is also related to the liquid fraction f_l [15]. The liquid fraction was assumed to be linearly varying with temperature:

$$f_l = \begin{cases} 1 & T > T_1 \\ \frac{T-T_s}{T_1-T_s} & T_1 \geq T \geq T_s \\ 0 & T < T_s, \end{cases} \quad (4)$$

where T_1 and T_s represent the liquidus and the solidus temperature of the melt liquid, respectively.

To track the shape of the metal surface, the volume of fluid (VOF) method is used [17]. It solves an equation of the volume fraction of metal in a cell (F) as:

$$\frac{\partial F}{\partial t} + (\vec{U} \cdot \nabla)F = 0, \quad (5)$$

where the VOF value of 1 ($F=1$) represents the liquid metal or solid metal, while the VOF value of 0 represents air. To neglect the friction effect of vapor and air, the viscosity of the gas is set to 0. Other physical parameters are interpolated based on the VOF value [17]. With the VOF method, the Weymouth–Yue scheme is adopted for multidimensional advection [18] and the piecewise linear interface construction (PLIC) method is used to reconstruct the free surface [19].

For the hydromechanics boundary condition of the keyhole and weld pool, important physical factors, including the Marangoni force, the recoil pressure and the surface tension, are considered together. Using a balanced-force algorithm to suppress the parasitic currents [20–22], the coupled term is expressed as:

$$F_s = (\sigma\kappa\vec{n} + \sigma_T\nabla_{||}T + P_s \cdot \vec{n})\delta_s, \quad (6)$$

where δ_s is a Dirac delta function, σ_T is the thermal-capillary force coefficient and P_s is the recoil pressure. Details can be found for the balanced-force algorithm in literature [20–22]. In particular, for the general strong evaporation in HP welding, the recoil pressure should be treated carefully. Here, a recent improved surface pressure model is adopted [23, 24], which can be expressed as:

$$P_s(T_{fs}) = \begin{cases} P_{amb} & 0 \leq T_{fs} < T_L \\ \frac{1+\beta_R}{2} P_0 \exp\left(\frac{\Delta H_v}{k_B T_v} \left(1 - \frac{T_v}{T_{fs}}\right)\right) & +\infty > T_{fs} \geq T_R \\ P_c(T_{fs}) & T_L \leq T_{fs} < T_R \end{cases}, \quad (7)$$

where P_{amb} is the ambient pressure, K_B is the Boltzmann constant, T_v is the boiling point, P_0 is the atmospheric

pressure, T_{fs} is the keyhole surface temperature, $p_c(T_{fs})$ is a smooth cubic interpolation curve, and T_L and T_R are the temperatures of the two tangent points between the smooth curve $p_c(T_{fs})$ with the ambient line and the recoil pressure curve. The parameters of the surface pressure model are referred to in [23].

For the thermodynamics boundary condition of the keyhole and weld pool, the multiple reflections of the laser beam on the metal surface is calculated with a robust ray tracing algorithm [25]. The laser beam energy distribution is modeled as a Gaussian function:

$$I_0(r, z) = 3P/(\pi R^2) \exp(-3(r^2)/R^2), \quad (8)$$

where R is the beam radius, and P is the laser power. With the ray tracing algorithm, the laser beam is divided into many bundles initially, where there are about 16 bundles in a finest cell for efficiency without a reduction of accuracy. The bundle has its direction (\vec{I}_0) and starting point coordinate. Along the direction of the propagation of the bundle, the nearest surface cell from the starting point is determined to absorb part of the bundle energy. The rest of the energy is carried by the reflected bundle, where the direction of the reflected bundle (\vec{I}_{n+1}) is calculated according to the law of reflection:

$$\vec{I}_{n+1} = \vec{I}_n + 2(-\vec{I}_n \cdot \vec{n})\vec{n}, \quad (9)$$

where \vec{I}_n is the unit vector of incident bundle and \vec{n} is the unit normal vector of the point on the metal surface and calculated with the mixed-Youngs-centered scheme under the VOF method [26]. The energy of each bundle is absorbed following Fresnel absorption formula [25], and the Fresnel absorption coefficient is

$$\alpha_{Fr}(\theta) = 1 - \frac{1}{2} \left(\frac{1 + (1 - \epsilon \cos \theta)^2}{1 + (1 + \epsilon \cos \theta)^2} + \frac{\epsilon^2 - 2\epsilon \cos \theta + 2\cos^2 \theta}{\epsilon^2 + 2\epsilon \cos \theta + 2\cos^2 \theta} \right). \quad (10)$$

where θ is the angle between the incident beam and the normal vector of surface cell, and ϵ is a coefficient related to the types of lasers. From above, the heat flux on metal surface from laser beam irradiation can be determined by

$$q = I_0(r, z) (\vec{I}_0 \cdot \vec{n}) \alpha_{Fr}(\theta_0) + \sum_{n=1}^m I_n(r, z) (\vec{I}_n \cdot \vec{n}) \alpha_{Fr}(\theta_n). \quad (11)$$

As the heat flux from laser beam irradiation on the metal surface is determined, a Dirac delta function is used to transform the heat flux of laser beam irradiation to a body heat source term (Q) added on the right hand side of Eq. 3. The transformation, adopted in many independent studies [27, 28], is also able to redistribute the energy absorbed by a cell and greatly simplify the calculation process without reducing the computational accuracy. The reason of redistributing

the energy is mainly for numerically smoothing and can be found in literature [27, 29]. After the transformation, the body heat source is written as,

$$Q = q \cdot \delta_s, \tag{12}$$

where using the VOF method, δ_s is determined by

$$\delta_s = \nabla F. \tag{13}$$

To determine the other thermal boundaries of the metal surface, cooling by thermal radiation and evaporation were applied according to the following expression:

$$\lambda \frac{\partial T}{\partial n} = -\epsilon_r \sigma_s (T^4 - T_\infty^4) - \rho V_{\text{evp}} L_v, \tag{14}$$

where ϵ_r is the emissivity, σ_s is the Stefan–Boltzmann constant, T_∞ is the ambient temperature, V_{evp} is the the surface recession speed due to evaporation, and L_v is the evaporation latent heat [28]. When calculating the temperature field, a robust temperature compensation method [25] was used to treat the evaporation heat and the fusion latent heat. In the present work, the fusion latent heat (L_f) of 304 stainless steel is found in previous studies [24].

In particular, an adaptive grid method for efficient simulation is adopted, taking the temperature and the VOF value into account to control the mesh refinement [20]. The accuracy of the used mesh adaption was checked and confirmed in previous tests. A computational flow chart (Fig. 3) is given to explain the mesh refinement process. In each time step of the computation, the reconstructed values of the physical fields such as temperature and VOF value, by interpolation or prolongation, are compared with the real values at each grid to judge the mesh refinement. That any one of the differences ($D(T)$ and $D(F)$ shown in Fig. 3) is bigger than the tolerance indicated that mesh refinement is needed. Only when all the differences are bigger than the corresponding tolerances, the mesh is coarsened. The way of reconstruction is dependent, for example, the virtual temperature value is easily linear interpolated and the VOF

value is reconstructed by considering geometric information. Some references can help the readers understand the mesh refinement method in detail [20].

In the present work, the computational domains were set to 20 mm × 8 mm × 8 mm for reducing the time consumed, as shown in Fig. 4. The lower part was 304 stainless steel with 15 mm thickness, and the upper part was air. At first, the grid was uniform with 500 μm sized length for efficiently tracking the flat surface of base metal. During the subsequent calculation process, the adaptive mesh refinement subroutine was invoked dynamically. The minimum size of the grid was set to 40 μm to capture the formation of fine spatters, as shown in Fig. 4. If using a uniform grid, the number of grids could be up to 2×10^7 . With the adaptive mesh refinement method, the number of grids was reduced to approximately 2×10^6 . About 80% of the time consumption was saved after testing. Under the tested adaptive mesh strategy, the simulations took about 15 h to complete a 60-ms laser welding process by using our homemade procedure in parallel on a small workstation (2.20 GHz CPU, 16 cores). The physical parameters used in the simulation are shown in the Table 2 [20, 30].

3 Results and discussion

3.1 A common spatter in HP laser welding-LBiS

Spatter is a serious defect in HP laser welding. Based on a recently developed comprehensive model and an adaptive mesh refinement method [16], we successfully visualized spatter behaviors as well as keyhole and weld pool dynamic behaviors in the 10 kW fiber laser welding of typical 304 stainless steel. The evolutions of the keyhole free surface, as well as temperature and velocity distributions at a welding speed of 1.0 m/min (process number 1), are shown in Fig. 5 and video 1. During the welding process, many spatters always ejected from the keyhole. The size of the

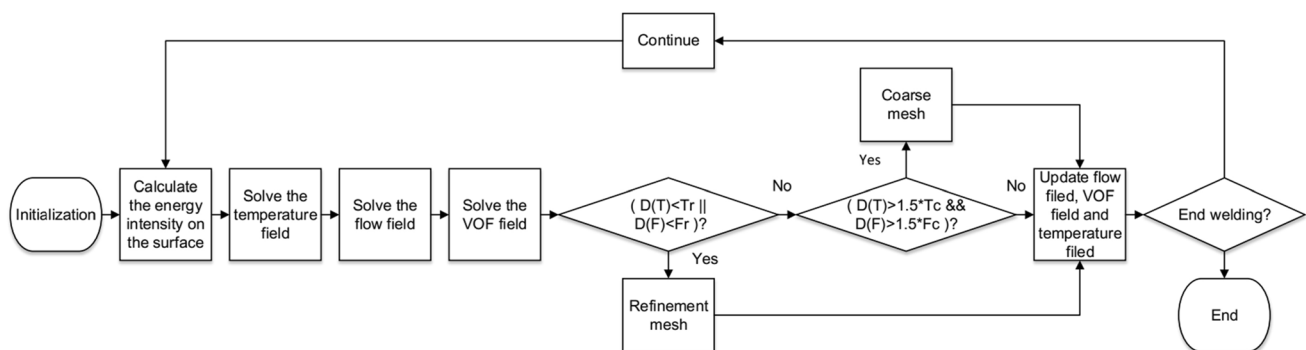


Fig. 3 Flowchart of the calculation

Fig. 4 Calculation domain and adaptive meshing. **a** Calculation domain; **b** top view of the mesh on the metal surface at 0 ms; **c** top view of the mesh on the metal surface at 0.05 ms

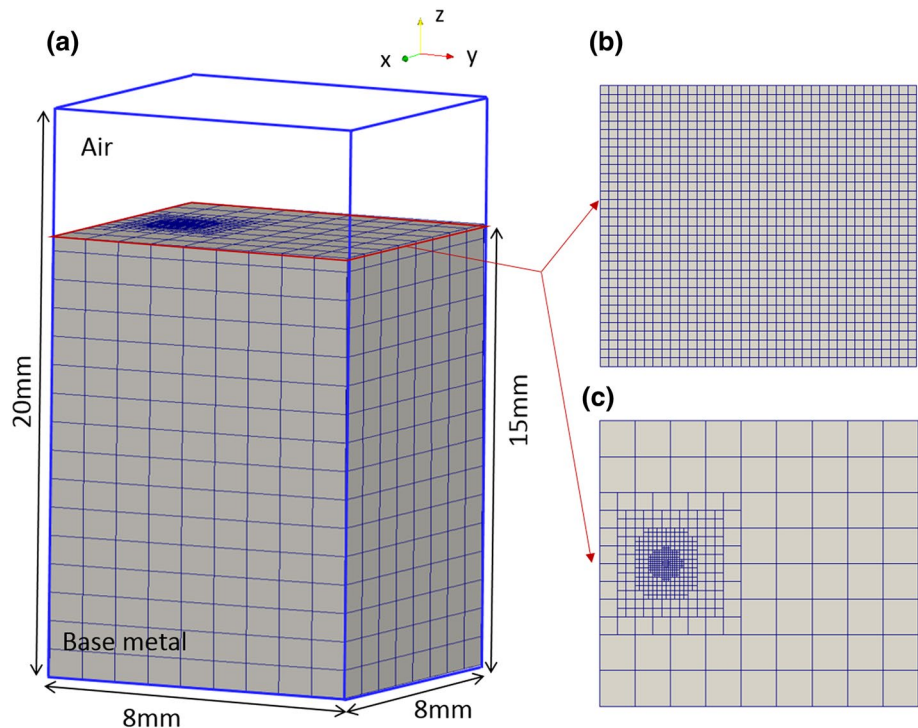


Table 2 Physical parameters used in the simulations

Physical parameters	Units	Value
Density ρ	kg m^{-3}	7200
Thermal conductivity coefficient k	$\text{W m}^{-1} \text{K}^{-1}$	35 (298 K)
Specific heat C_p	$\text{J kg}^{-1} \text{K}^{-1}$	760 (298 K)
Kinematic viscosity μ	$\text{kg m}^{-1} \text{s}^{-1}$	0.006
Latent heat of fusion C_f	J kg^{-1}	6.0×10^5
Latent heat of evaporation C_v	J kg^{-1}	6.52×10^6
Solidus temperature T_s	K	1727
Liquidus temperature T_l	K	1697
Evaporation temperature T_v	K	3100
Surface tension coefficient σ	N m^{-1}	1.0
Thermal-capillary force coefficient σ_T	$\text{N m}^{-1} \text{K}^{-1}$	-0.43×10^{-3}

spatters was usually very small. The diameter was 200 μm or smaller, within the range of traditional observation results (20–500 μm) [7, 8]. Additionally, the main ejection direction of the spatters was upward around the keyhole opening. Moreover, as shown in Fig. 5e, the temperature distribution of the keyhole wall was far from uniform. The high temperature, which often occurred on the top parts of the keyhole humps, reached 3200 K or even higher (under standard atmospheric pressure the boiling point of the material used is 3100 K). Thus, intensive local boiling occurred at those locations, causing high-speed molten liquid (10 m/s or even larger) to spray in all directions (Fig. 5e). Since the friction

effect of the vapor plume on the molten liquid was deliberately neglected in the simulations, the predicted spatters were supposed to be closely related to the intensive local boiling effect.

To further investigate the formation of the spatters, we numerically visualized the evolution of the velocity of molten liquid near the keyhole wall (process number 1), as shown in Fig. 6 and video 2. Many humps occurred on the keyhole wall. At a welding time of 13.016 ms, intense localized boiling occurred at the high temperature position of the hump (more than 3100 K) on the keyhole wall (Fig. 6a). The boiling molten liquid with a high speed of about 10 m/s sputtered around, which coincided with the experimental observation [31]. As the welding proceeded, the humps moved upward or downward and some parts of the upward boiling molten liquid ejected to the keyhole opening (Fig. 6b). The ejection speed and the temperature of the molten liquid jet were about 6.4 m/s and 2800 K, respectively. At a welding time of 14.675 ms, the molten liquid jet sprayed out of the keyhole and a separation occurred (Fig. 6c). The temperature of the molten liquid jet with a speed of 5.2 m/s was reduced to 2400 K. As the welding time went to 15.988 ms, the tip part of the broken molten liquid jet formed a spatter with a temperature of about 2200 K, and a speed of about 4 m/s (Fig. 6d). The diameter was about 200 μm if the spatter was taken as a droplet. Based on the above results, we can roughly classify the formation process of the spatter into four stages: intensive local boiling (Fig. 6a), strong jet (Fig. 6b), liquid separation (Fig. 6c), and spatter formation

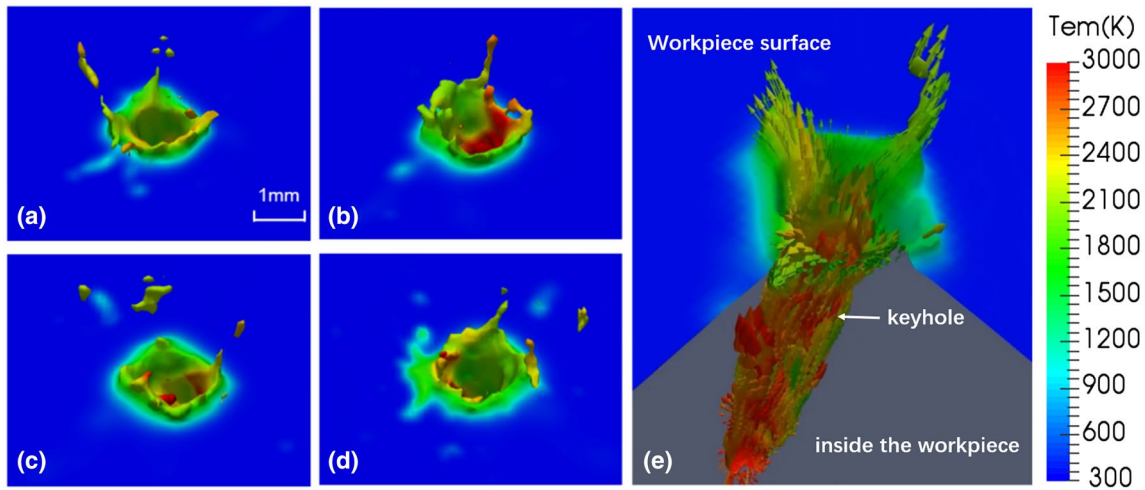


Fig. 5 Evolutions of spatter behaviors during the welding process: **a** 6.2 ms; **b** 8.2 ms; **c** 10.2 ms; **d** 12.2 ms; **e** the temperature distribution of the keyhole

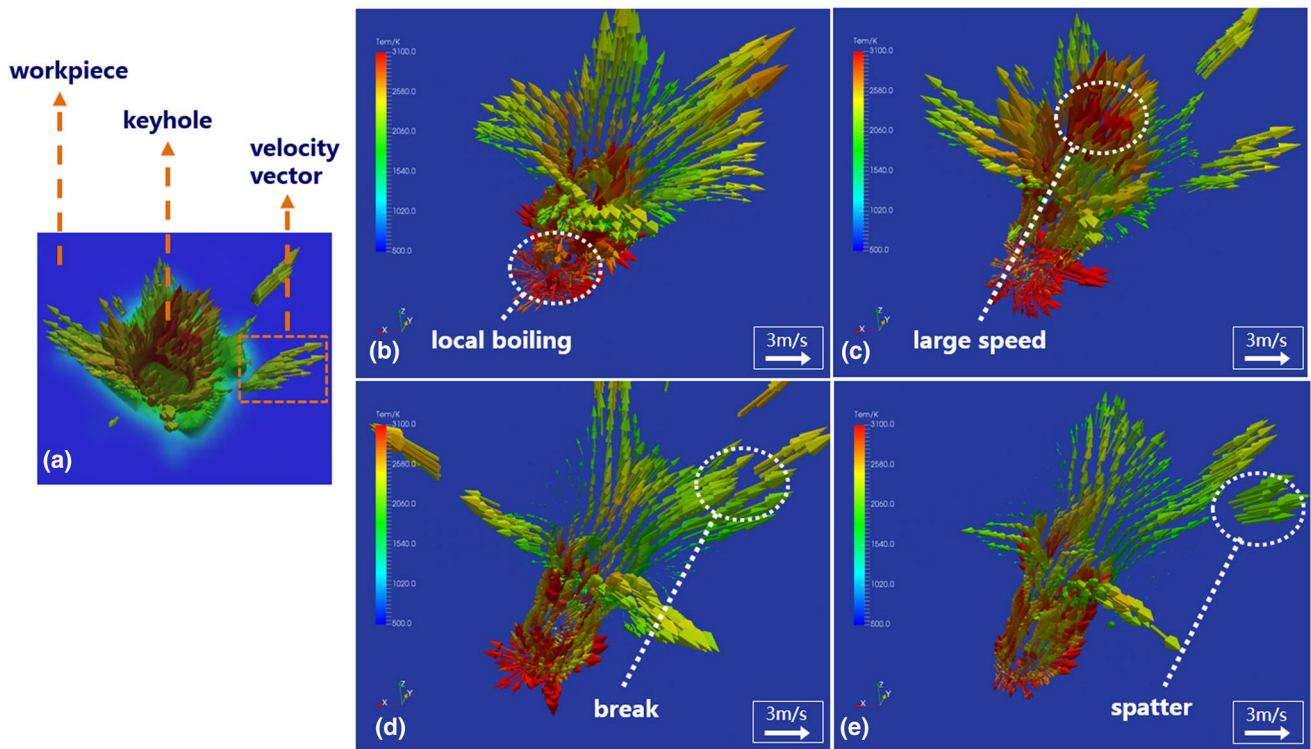


Fig. 6 The temperature and velocity characteristics during the formation of spatters at different times. **a** Top view of the temperature and velocity distribution, **b** 13.016 ms; **c** 13.975 ms; **d** 14.675 ms; **e** 15.988 ms

(Fig. 6d). According to the characteristics of the spatter formation, we call this spatter a localized boiling-induced spatter (LBiS). The period of LBiS formation was about 2–3 ms. As multiple local intense boiling could occur on the keyhole wall at the same time, the frequency was hard to determine. It was roughly estimated that there was one spatter per millisecond. In fact, the occurrences of intense

localized boiling as well as LBiS forming outside the keyhole have been reported by previous experimental research [7, 12, 32]. However, the formation process and the quantitative dynamic characteristics of LBiS have not been reported. To the best of the authors’ knowledge, this study was the first to quantitatively predict the entire formation process of LBiS using numerical simulations.

3.2 Characteristics of LBiS outside keyhole

To validate the proposed model and simulation result experimentally and further characterize LBiS, a series of HP laser welding experiments were performed (process numbers 1–7). Comparisons of the weld dimensions are shown in Fig. 7. The predicted weld cross section was very consistent with the experimental result (Fig. 7a). Additionally, the penetration depths and widths of the predicted results also agreed well with the experimental data (Fig. 4b, c). The simulated molten pool flow results are consistent with the experimental results of Katayama et al. [33]. These agreements indicate that our adopted mathematical model and simulation results are reliable.

Figure 8 shows high-speed images at a welding time of 115 ms (quasi-steady state) for HP laser welding of typical 304 stainless steel under different welding speeds (process numbers 2–5). The corresponding weld-bead surfaces are

shown in Table 3 (process numbers 1–5). A mass of spatters occurred during the welding process. The size and the movement direction were both varied (Fig. 8), which is consistent with previous experimental research [34, 35]. Serious spatter defects and poor surface quality of the weld beads were easily found, as shown in Table 3. Here, we mainly paid attention to a kind of small size spatter, the numbers of which were large in HP laser welding. It was found that many spatters with a diameter of about 200 μm or even smaller sprayed above the workpiece (Fig. 8) and finally formed spatter defects at the surface of the weld beads (Table 3). Furthermore, these kinds of spatters usually occurred at the upper position near the keyhole opening during the welding process (Fig. 8). The above-mentioned characteristics of the spatters are exactly the same as those of the predicted LBiS.

As mentioned in Sect. 3.1, the LBiS was different for the spatters caused by the dragging effects of the vapor plume in laser welding. It can be easily seen that if the dragging effect

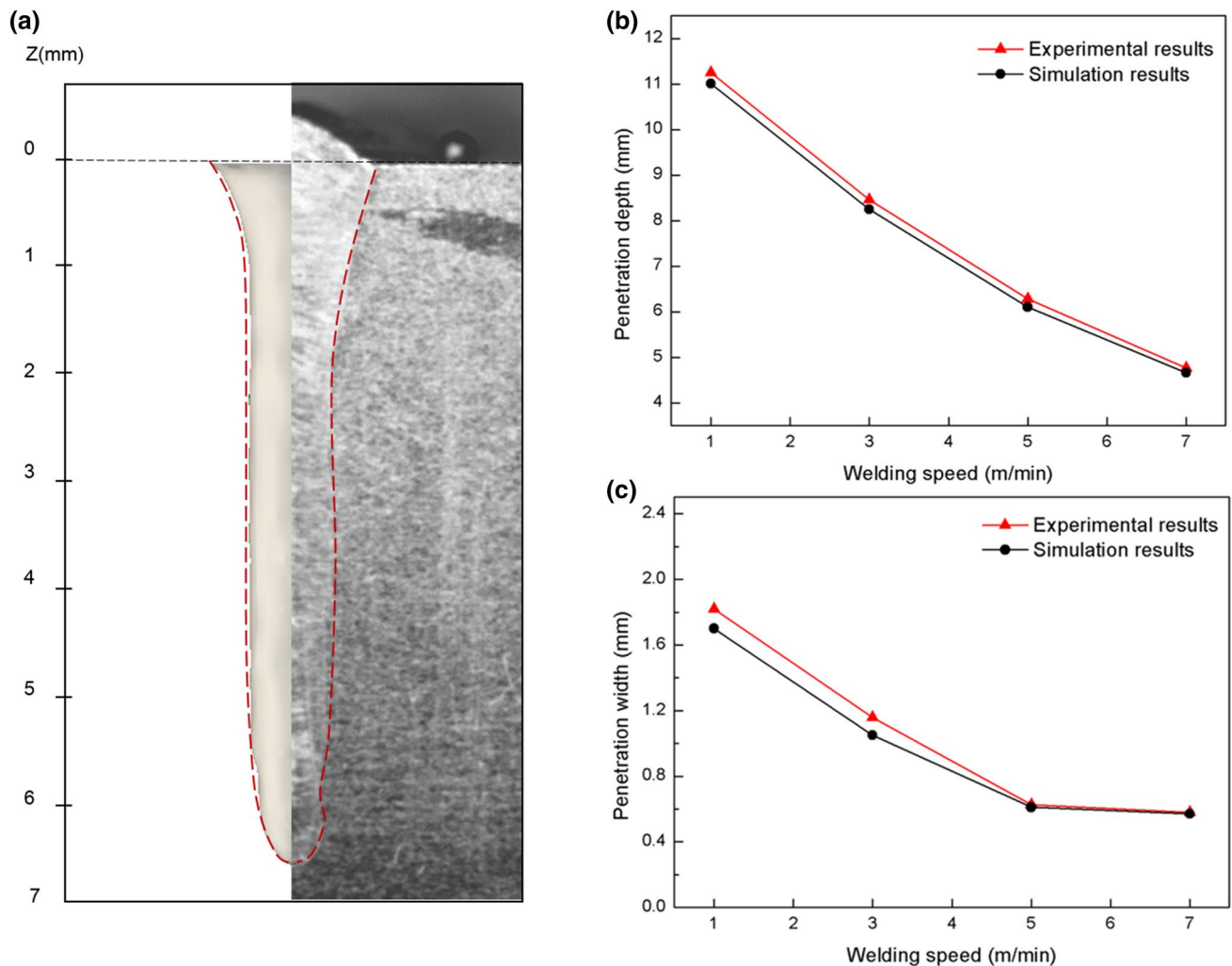


Fig. 7 Comparisons of weld dimensions between simulation and experimental results: **a** weld cross section (process number 3); **b** penetration depth (process numbers 1–4); **c** penetration width (process numbers 1–4)

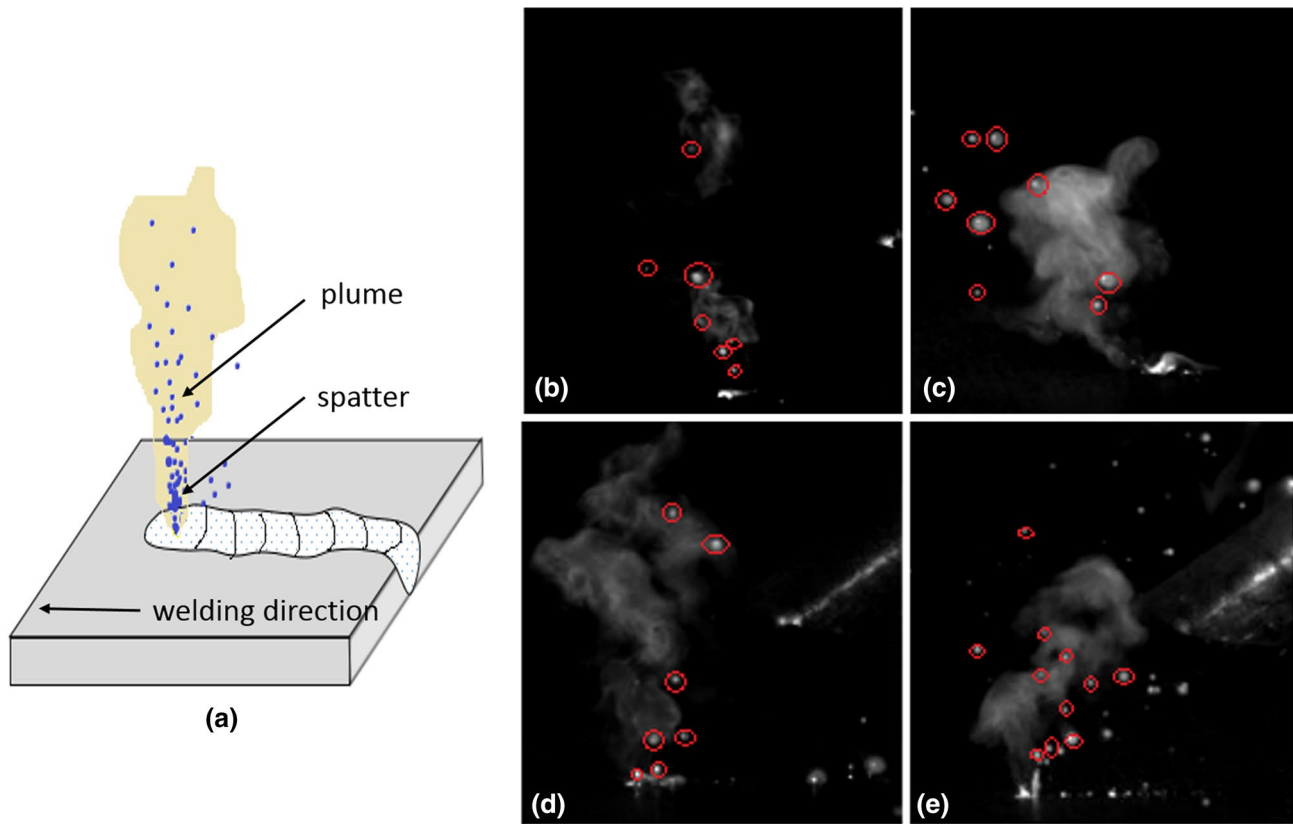


Fig. 8 Spatter pictures at different welding speeds (process numbers 2–5): **a** $V=3$ m/min; **b** $V=5$ m/min; **c** $V=7$ m/min; **d** $V=9$ m/min

of the vapor plume dominates the formation of spatters under a large welding speed, the ejection direction of the spatters would be backward (contrary to the welding direction). To further ensure the common existence of LBiS in experiments and real industrial activity during HP laser welding, we observed the spatters under large welding speeds, as shown in Fig. 9 (process numbers 6, 7). It was found that even when the welding speed increased to 12 and 15 m/min, there were still some small upward spatters at the upper position near the keyhole opening. The above-mentioned characteristics of the small spatters in the experiments are consistent with the predicted LBiS. This demonstrated that LBiS is also a common kind of spatter, which we should pay more attention to and reduce and eliminate in HP laser welding.

3.3 Physical mechanism of LBiS formation

To decrease the spatter defects, we further analyzed the formation mechanisms of LBiS, based on the above experimental and simulation data for the HP laser welding process. First, intense localized boiling occurred on the top part of the keyhole wall due to the direct irradiation of the laser beams. This establishes the original energy for the spatter formation. As a result, a high-speed (5 m/s or even larger)

boiling molten liquid jet forms, driven by large recoil pressure due to violent local evaporation. When the molten liquid jet ejects from the keyhole opening, its upward speed can still be very large, as seen in the approximately 4 m/s jet in Fig. 6c. The kinetic energy of the molten liquid jet is much larger than its surface energy, which is about 1000:1. Therefore, the local molten liquid will break into two parts and then separate. As the welding continues, the tip section of the small droplet moves faster without the dragging effect of the surface tension on the other section and finally the spatter forms. The mechanism of LBiS is well presented in videos 1 and 2.

Obviously, the formation mechanism of LBiS is different from the current explanation that the spatter formation is dominated by the dragging effects of high-speed vapor plume during laser welding [36, 37]. As mentioned above, if the dragging effect of the vapor plume dominates the formation process, the ejection direction of the spatters would be backward (contrary to the welding direction) under a large welding speed, which is not consistent with the observed upward spatters in high-speed HP laser welding (Fig. 9). In addition, note that a Knudsen layer exists near the evaporation or condensation interface, and the dragging effects of vapor plume were obviously weakened by this

Table 3 Weld bead surface appearances at different welding speeds











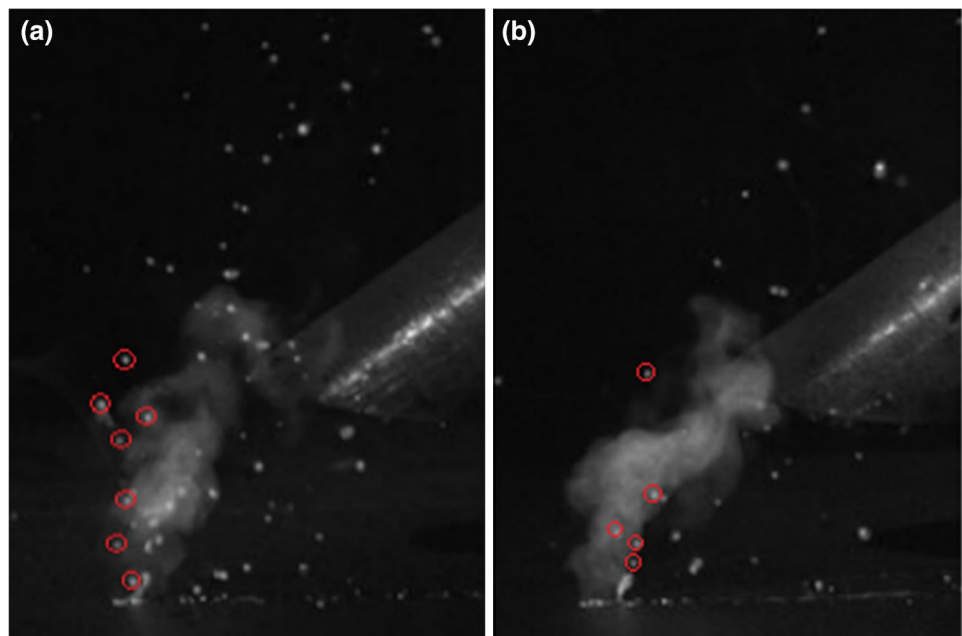
Welding speed (m/min)	Weld bead surface appearance	
1		
3		
5		
7		
9		

Fig. 9 Upward spatters during high-speed welding. **a** $V=12$ m/min; **b** $V=15$ m/min

pressure-discontinuous buffer zone [38]. Furthermore, the high-speed vapor plume caused by the violent local evaporation on the front and back keyhole walls might meet inside the keyhole, which would also weaken the dragging effect

[39, 40]. That is because the drag force of the gas on the liquid is directly dependent on the difference of gas–liquid velocity. When the gas encounters and reduces the speed, the dragging effect is weakened. Moreover, previous research

has also discussed the fact that the boiling-induced recoil pressure played an important role in spatter formation [7, 12, 32]. Note that in the present study, our adopted model, which was validated by experiments and did not consider the dragging effect of the vapor plume on the molten liquid, successfully predicted the common LBiS in HP laser welding. Therefore, the LBiS is dominantly caused by an intense localized boiling effect. In summary, to the best of the authors' knowledge, this study is the first to quantitatively clarify the formation process and mechanism of LBiS in HP laser welding. Our findings can serve as an important theoretical tool for the field of spatter defects and can help improve understanding of the HP laser welding process.

3.4 A simple theory for LBiS based on energy conservation

To study the conditions for the formation of LBiS in HP laser welding, we proposed a theoretical model to describe the spatter and introduced a critical condition based on the principle of conservation of energy. During the welding process, the molten liquid in the weld pool is mainly subjected to the recoil pressure, inertial force, thermal capillary force, surface tension, and viscous force that keep the liquid droplets from leaving the liquid surface. Since the recoil pressure F_c , surface tension F_s , and viscous force F_f all play a major role in droplet motion during HP welding, we only considered those three forces, adding the gravity G in the theoretical model of LBiS. We denoted the metal liquid density as ρ , the viscosity coefficient as μ , the surface tension coefficient as σ , and the thickness of the flowing molten liquid film as Φ . A droplet at any position had an initial velocity (in any direction) driven by the initial recoil pressure. Assuming that the droplet to be studied was spherical and moved upward with a diameter of d , the initial velocity of movement was v and the distance from the initial position to the keyhole opening was h . When the droplet moved upward to the keyhole opening, the spatter volume was $V = \frac{\pi}{6}d^3$, the exercise time was $t \approx \frac{2h}{v}$, and the kinetic energy was, expressed as,

$$E_k = \frac{\pi}{12} \rho d^3 v^2. \tag{15}$$

The energy dissipated by the viscous effect was expressed as,

$$E_f = \frac{\pi}{6} d^3 \mu \left(\frac{v}{\Phi}\right)^2 \left(\frac{2h}{v}\right). \tag{16}$$

The surface tension energy was expressed as,

$$E_s = \pi d^2 \sigma. \tag{17}$$

The gravity work was expressed as,

$$E_p = \frac{\pi}{6} d^3 \rho gh. \tag{18}$$

When the condition $E_k > E_f + E_s + E_p$ was established; namely,

$$\frac{\pi}{12} \rho d^3 v^2 > \frac{\pi}{6} d^3 \mu \left(\frac{v}{\Phi}\right)^2 \left(\frac{2h}{v}\right) + \pi d^2 \sigma + \frac{\pi}{6} d^3 \rho gh, \tag{19}$$

the spatter was formed.

From Eq. (11), the main dimensionless numbers that relate to the formation of LBiS are $Re = \frac{\rho \Phi v}{\mu}$ and $We = \frac{\rho \Phi v^2}{\sigma}$.

Thus, Eq. (11) can be simplified as

$$\frac{1}{12} > \left(\frac{h}{3\Phi}\right) \frac{1}{Re} + \left(\frac{\Phi}{d}\right) \frac{1}{We} + \frac{gh}{6v^2}. \tag{20}$$

Based on Eq. (12), we can define a dimensionless number ξ to characterize the initial condition of the LBiS formation $\left(\xi = \left(\frac{4h}{\Phi}\right) \frac{1}{Re} + \left(\frac{12\Phi}{d}\right) \frac{1}{We} + \frac{2gh}{v^2}\right)$. When $\xi < 1$, the molten liquid can separate from the liquid surface to form a spatter. It should be noted that the spatter was assumed to be a spherical shape with a constant radius of curvature in this study. When the droplet moved upward, the longer the moving distance was, the easier was the scatter of the droplet. Therefore, the spatters studied in this paper were mainly the small ones in the upper part of the keyhole. From Eq. (12), it is apparent that spatter formation is related to Re , We , spatter position h , spatter diameter d , and the flowing liquid film thickness Φ in the flowing process. The smaller the Re , the more the viscous force has an effect on the droplet flow instead of the inertia. The droplet flow velocity decays due to the viscous force, and the droplet does not easily fly out of the liquid surface to form a spatter. The larger the We , the more the effect of the surface tension on the droplet flow is less than the inertia. The droplet flies out of the liquid surface under inertial action to form a spatter. The larger the h , the more the viscous force and the gravity work when the droplet moves upward, and the less likely the droplet is to form a spatter. The smaller the d , the more the droplets do not bulge when they reach the liquid level, and the liquid surface is less likely to form folds, so the spatter is difficult to form. The smaller the Φ , the greater the work of the sticking force will be when the droplet moves upward, and there is less possibility to splash and form the spatter.

Table 4 lists the welding parameters under different conditions in simulations and the corresponding spatter numbers ξ calculated by the determination formula. Figure 10 shows the relationship between the values of the dimensionless number ξ and the situations of spatter formation using the data from Table 4. When the corresponding dimensionless number $\xi > 1$, almost no spatters occurred during the welding process, while with the dimensionless number $\xi < 1$, spatters occurred. This demonstrates that the predicted spatter formation situation is very consistent with the result predicted by Eq. (12). In

Table 4 Statistical results of the spatter number ξ

Welding speed - (m/min)	Liquid film thickness Φ (m)	Spatter speed v (m/s)	Spatter position h (m)	Spatter diameter d (m)	Spatter number ξ -	Whether to form spatter (Filled: Yes; Not Filled: No)
1	0.00015	5.45	0.0008	0.0004	0.1902	●
		5.82	0.002	0.0004	0.1986	●
		4.98	0.003	0.0003	0.3582	●
		5.63	0.0042	0.0006	0.21576	●
		5.46	0.003	0.0005	0.21564	●
		5.28	0.01	0.0001	0.99804	○
		4.76	0.008	0.0001	1.13184	○
		5.21	0.0073	0.0001	0.94452	○
		4.35	0.0082	0.0001	1.33632	○
		4.28	0.0068	0.0001	1.32732	○
3	0.00013	4.98	0.0006	0.0004	0.22548	▲
		4.86	0.0016	0.0002	0.4884	▲
		5.11	0.0027	0.0003	0.35964	▲
		5.02	0.0033	0.0005	0.28848	▲
		4.63	0.004	0.0003	0.48156	▲
		4.32	0.006	0.0001	1.3458	△
		4.15	0.0056	0.0001	1.42752	△
		4.26	0.0048	0.0001	1.32444	△
		4.44	0.0053	0.0001	1.25004	△
		4.86	0.0061	0.0001	1.0944	△
5	0.0001	4.36	0.0004	0.0002	0.55668	■
		4.28	0.001	0.0002	0.62388	■
		4.43	0.0022	0.0002	0.67524	■
		4.67	0.002	0.0002	0.60132	■
		4.32	0.0025	0.0003	0.5502	■
		4.16	0.0043	0.0001	1.50036	□
		4.33	0.0044	0.0001	1.40556	□
		3.93	0.0046	0.0001	1.68516	□
		4.16	0.0046	0.0001	1.5084	□
		4.38	0.0048	0.0001	1.40796	□

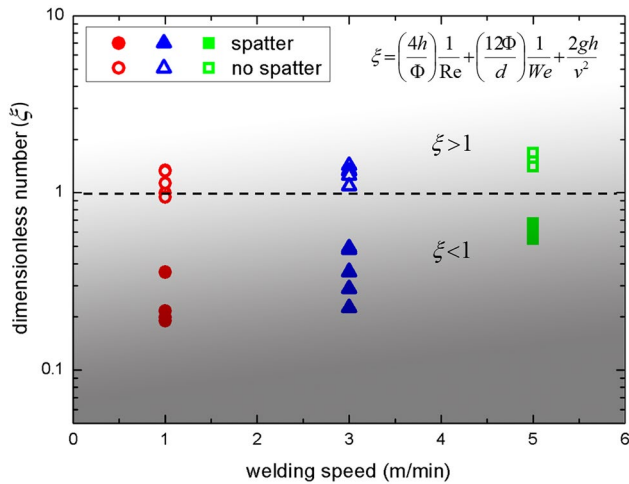


Fig. 10 Dimensionless spatter numbers under different welding speeds

addition, as the welding speed increased, the dimensionless number ξ corresponding to the formation of spatters generally increased, but it was always less than 1. This indicates that LBiS formation is more difficult as the welding speed increases, which has a reasonable agreement with the proposed formation mechanism of LBiS.

Consequently, in this study we are the first to quantitatively investigate the formation and characteristics of LBiS and systematically clarify the mechanisms of LBiS formation in HP laser welding using a comprehensive adaptive mesh refinement model combined with an experimental method. Based on the law of energy conservation and incorporating the main kinetic factors, such as recoil pressure, surface tension, and viscous force, we proposed a theoretical model to characterize the situation of LBiS formation. The predicted situation of the LBiS formation showed good agreement with the 30 sets of statistical data (Table 4) and the formation mechanism of LBiS. Our methods and findings can help deepen the understanding of spatter during HP laser welding. Furthermore, the proposed theoretical model can be used to judge whether LBiS is formed during the welding process, which can help guide future process optimization.

4 Conclusion

In this paper, we systematically investigated the characteristics, formation process, mechanisms and conditions of LBiS in HP (10 kW) fiber laser welding of typical 304 stainless steel, using a combination of the methods of numerical modeling, experiments and theoretical analysis. The major findings are shown as follows.

1. Based on a three-dimensional comprehensive model and an adaptive mesh-refinement method, the dynamic behaviors of the keyhole and the weld pool, especially their formation and characteristics, were quantitatively observed and analyzed. The predicted LBiS behaviors, as well as the weld dimensions, were consistent with the experimental and literature data.
2. LBiS usually had an upward velocity direction and occurred at the upper position outside the keyhole. Its diameter was about 200 μm , or even less if the spatter was taken as a spherical droplet. The formation process of LBiS included four steps: intensive local boiling, strong jet, liquid separation, and spatter formation. Its formation period was about 2–3 ms.
3. Intense localized boiling occurred on the mesoscopic humps of the keyhole wall, provided the origin kinetic energy for the boiling molten liquid was LBiS. When the molten liquid jet was ejected from the keyhole opening, and its kinetic energy was larger than its surface energy, the molten liquid jet broke into two parts and LBiS was formed.
4. A significant formula was successfully deduced to judge the formation condition of LBiS. LBiS occurred only when the dimensionless number ξ was less than 1. In summary, our methods and findings can serve as a tool or guide to a supplementary understanding of the physical formation of spatter defects and the optimization of the welding process during the HP laser-welding process.

Acknowledgements This research was financially supported by the National Natural Science Foundation of China (NSFC) (No. 51675202) and the Key R&D Projects (National Key projects) (No. 2017YFE0100100).

References

1. M. Mizutani, S. Katayama, Y. Kawahito, Elucidation of high-power fibre laser welding phenomena of stainless steel and effect of factors on weld geometry. *J. Phys. D Appl. Phys.* **40**(19), 5854 (2007)
2. Y. Kawahito, M. Mizutani, S. Katayama, High quality welding of stainless steel with 10 kw high power fibre laser. *Sci. Technol. Weld. Join.* **14**(4), 288–294 (2009)
3. H. Park, S. Rhee, Analysis of mechanism of plasma and spatter in CO_2 laser welding of galvanized steel. *Opt. Laser Technol.* **31**(31), 119–126 (1999)
4. J. Volpp, Formation mechanisms of pores and spatters during laser deep penetration welding. *J. Laser Appl.* **30**(1), 012002 (2018)
5. J. Weberpals, F. Dausinger, Fundamental understanding of spatter behavior at laser welding of steel. Proceedings of the 27th ICALEO conference, 704 (2008)
6. S. Katayama, Y. Kawahito, Elucidation of phenomena in high-power fiber laser welding and development of prevention

- procedures of welding defects. Proc. SPIE Int. Soc. Opt. Eng. **146**(1), 124–126 (2009)
7. D. Wu, X. Hua, F. Li, L. Huang, Understanding of spatter formation in fiber laser welding of 5083 aluminum alloy. Int. J. Heat Mass Transfer **113**, 730–740 (2017)
 8. A.F.H. Kaplan, J. Powell, Spatter in laser welding. J. Laser Appl. **23**(23), 3337–3344 (2011)
 9. A.F.H. Kaplan, I. Eriksson, J. Powell, Measurements of fluid flow on keyhole front during laser welding. Sci. Technol. Weld. Join. **16**(7), 636–641 (2011)
 10. A. Matsunawa, V. Semak, The simulation of front keyhole wall dynamics during laser welding. J. Phys. D Appl. Phys. **30**(5), 798 (1997)
 11. A. Matsunawa, N. Seto, J.D. Kim, S. Katayama, Dynamics of keyhole and molten pool in high-power CO₂ laser welding. J. Laser Appl. **10**(6), 247–254 (2000)
 12. M.J. Zhang, G.Y. Chen, Y. Zhou, S.C. Li, H. Deng, Observation of spatter formation mechanisms in high-power fiber laser welding of thick plate. Appl. Surf. Sci. **280**(9), 868–875 (2013)
 13. S. Pang, X. Chen, X. Shao, S. Gong, J. Xiao, Dynamics of vapor plume in transient keyhole during laser welding of stainless steel: local evaporation, plume swing and gas entrapment into porosity. Opt. Lasers Eng. **82**, 28–40 (2016)
 14. S. Pang, W. Chen, W. Wang, A quantitative model of keyhole instability induced porosity in laser welding of titanium alloy. Metall. Mater. Trans. A **45**(6), 2808–2818 (2014)
 15. R. Rai, T.D. Roy, Tailoring weld geometry during keyhole mode laser welding using a genetic algorithm and a heat transfer model. J. Phys. D Appl. Phys. **39**(6), 1257–1266 (2006)
 16. J. Zhou, H.L. Tsai, T.F. Lehnhoff, Investigation of transport phenomena and defect formation in pulsed laser keyhole welding of zinc-coated steels. J. Phys. D Appl. Phys. **39**(24), 5338 (2006)
 17. R. Scardovelli, S. Zaleski, Direct numerical simulation of free-surface and interfacial flow. Ann. Rev. Fluid Mech. **31**(1), 567–603 (1999)
 18. G.D. Weymouth, D.K.P. Yue, Conservative volume-of-fluid method for free-surface simulations on Cartesian-grids. J. Comput. Phys. **229**(8), 2853–2865 (2010)
 19. D.L. Youngs, Time-dependent Multi-material Flow with Large Fluid Distortion, in *Numerical Methods for Fluid Dynamics*, ed. by K.W. Morton, M.J. Baines (Academic, New York, 1982), p. 273
 20. R. Hu, S. Pang, X. Chen, L. Liang, X. Shao, An octree-based adaptive mesh refinement method for three dimensional modeling of keyhole mode laser welding. Int. J. Heat Mass Transfer **115**, 258–263 (2017)
 21. D. Fuster, A. Bagué, T. Boeck, Simulation of primary atomization with an octree adaptive mesh refinement and VOF method. Int. J. Multiph. Flow **35**(6), 550–565 (2009)
 22. M.M. Francois, S.J. Cummins, E.D. Dendy, A balanced-force algorithm for continuous and sharp interfacial surface tension models within a volume tracking framework. J. Comput. Phys. **213**(1), 141–173 (2006)
 23. S. Pang, K. Hirano, R. Fabbro, T. Jiang, Explanation of penetration depth variation during laser welding under variable ambient pressure. J. Laser Appl. **27**(2), 022007 (2015)
 24. S. Pang, X. Chen, J. Zhou, X. Shao, C. Wang, 3D transient multiphase model for keyhole, vapor plume, and weld pool dynamics in laser welding including the ambient pressure effect. Opt. Lasers Eng. **74**, 47–58 (2015)
 25. S. Pang, L. Chen, J. Zhou, Y. Yin, T. Chen, A three-dimensional sharp interface model for self-consistent keyhole and weld pool dynamics in deep penetration laser welding. J. Phys. D Appl. Phys. **44**(2), 025301 (2011)
 26. G.H. Miller, P. Colella, A conservative three-dimensional Eulerian method for coupled solid–fluid shock capturing. J. Comput. Phys. **183**(1), 26–82 (2002)
 27. Z.S. Saldi, *Marangoni driven free surface flows in liquid weld pools* (Delft University of Technology, Delft, 2012)
 28. H. Ki, J. Mazumder, P.S. Mohanty, Modeling of laser keyhole welding: Part I. Mathematical modeling, numerical methodology, role of recoil pressure, multiple reflections, and free surface evolution. Metall. Mater. Trans. A **33**(6), 1817–1830 (2002)
 29. W.I. Cho, S.J. Na, M.H. Cho, Numerical study of alloying element distribution in CO₂ laser–GMA hybrid welding. Comput. Mater. Sci. **49**(4), 792–800 (2010)
 30. X. He, J.T. Norris, P.W. Fuerschbach, Liquid metal expulsion during laser spot welding of 304 stainless steel. J. Phys. D Appl. Phys. **39**(3), 525 (2006)
 31. M.J. Zhang, G.Y. Chen, Observation of spatter formation mechanisms in high-power fiber laser welding of thick plate. Appl. Surf. Sci. **280**(9), 868–875 (2013)
 32. D. Wu, X. Hua, L. Huang, J. Zhao, Numerical simulation of spatter formation during fiber laser welding of 5083 aluminum alloy at full penetration condition. Opt. Laser Technol. **100**, 157–164 (2018)
 33. S. Katayama, Y. Kawahito, Elucidation of phenomena in high-power fiber laser welding and development of prevention procedures of welding defects, in *Fiber lasers VI: technology, systems, and applications. International Society for Optics and Photonics*, vol. 7195, 71951R (2009)
 34. F. Hugger, K. Hofmann, S. Kohl, M. Dobler, M. Schmidt, Spatter formation in laser beam welding using laser beam oscillation. Weld. World **59**(2), 165–172 (2015)
 35. S. Li, G. Chen, S. Katayama, Y. Zhang, Relationship between spatter formation and dynamic molten pool during high-power deep-penetration laser welding. Appl. Surf. Sci. **303**(6), 481–488 (2014)
 36. E.H. Amara, R. Fabbro, Modelling of gas jet effect on the melt pool movements during deep penetration laser welding. J. Phys. D Appl. Phys. **41**(41), 055503 (2008)
 37. R. Fabbro, M. Hamadou, F. Coste, Metallic vapor ejection effect on melt pool dynamics in deep penetration laser welding. J. Laser Appl. **16**(1), 859–870 (2004)
 38. Y.H. Zhang, X.J. Gu, R.W. Barber, D.R. Emerson, Capturing knudsen layer phenomena using a lattice boltzmann model. Phys. Rev. E Stat. Nonlinear Soft Matter Phys. **74**(2), 046704 (2006)
 39. E.H. Amara, R. Fabbro, F. Hamadi, Modeling of the melted bath movement induced by the vapor flow in deep penetration laser welding. J. Laser Appl. **18**(1), 2–11 (2006)
 40. V. Semak, A. Matsunawa, The role of recoil pressure in energy balance during laser materials processing. J. Phys. D Appl. Phys. **30**(18), 2541 (1999)